

On the design of piezoelectric MEMS microspeaker for the sound pressure level enhancement

Hsu-Hsiang Cheng^a, Sung-Cheng Lo^a, Zi-Rong Huang^a, Yi-Jia Wang^a, Mingching Wu^c, Weileun Fang^{a,b,*}

^a Power Mechanical Engineering, National Tsing Hua Univ., Hsinchu, Taiwan

^b Institute of NanoEngineering and MicroSystems, National Tsing Hua Univ., Hsinchu, Taiwan

^c Coretronic MEMS Corporation, Hsinchu, Taiwan



ARTICLE INFO

Article history:

Received 16 December 2019

Received in revised form 26 February 2020

Accepted 16 March 2020

Available online 20 April 2020

Keywords:

Piezoelectric

Microspeaker

PZT

Sound pressure level

ABSTRACT

This study aims to design and realize MEMS microspeakers with high sound pressure level (SPL) for in-ear applications. On the basis of high piezoelectric coefficient PZT thin film, the proposed suspension-spring and dual-electrode designs enhance the out-of-plane displacement of central diaphragm to improve low-frequency SPL. The preliminary tests show that both proposed single-curve and dual-curve spring designs have higher low-frequency SPL than that of the reference clamped diaphragm microspeaker. Measured in the standard ear simulator systems with 2 V_{pp} driving voltage, the proposed dual-curve spring design demonstrates good performance at low frequencies. At the resonant frequency of 1.85 kHz, the dual-curve spring design is 28 dB SPL higher than the clamped diaphragm. In addition, from 100 Hz to 3 kHz, more than 10 dB SPL enhancement is achieved. Furthermore, the total harmonic distortion (THD) of dual-curve spring design is less than 2% in most of the audio range. Compared with the published literature of piezoelectric MEMS microspeakers, this study shows a reasonable SPL with the smallest diaphragm area of 1 mm².

© 2020 Elsevier B.V. All rights reserved.

1. Introduction

The micro-electro-mechanical-systems (MEMS) technologies have been extensively adopted to fabricate chips of various applications, especially the micro sensors. However, the applications of micro actuators are still limited due to the small output force, displacement, etc. The Texas Instruments Digital Micromirror Device demonstrates the capability of MEMS actuator for optical modulation [1], and the SiTime shows the application of MEMS actuator for timing devices [2]. Presently, micro actuators have continuously attracted attentions in optical and acoustic devices [3–4]. In addition to microphones, speakers are another fundamental acoustic device in our daily life and also existing in many consumer electronics, for instance, the smartphones, portable laptops, and some in-ear applications like earphones and hearing aids. With the trend of miniaturization of electronic devices, several microspeakers have been developed by using the MEMS technologies [5–6]. According to the characteristics of micro fabrication technologies, MEMS microspeakers have two major advantages including the size

reduction and the capability of batch fabrication to lower the cost. It is expected that MEMS technologies will be promising approaches to realize microspeakers.

In general, the electromagnetic, electrostatic, and piezoelectric are three actuation approaches to drive MEMS microspeakers [7–13]. The electromagnetic force (Lorenz force) is the most common driving method adopted by the existing MEMS microspeakers. Since the electromagnetic microspeaker could contribute a larger driving force as well as diaphragm displacement, a better acoustic performance is achieved [7–10]. However, the fabrication processes are relatively complicate and generally the assembly of magnet is required. Such non-batched assembly process will lead to extra cost and efforts for electromagnetic MEMS microspeakers. More, as reported in [11–12], the standard CMOS processes are exploited to realize MEMS electrostatic microspeakers. In addition to the advantage of available foundry service, the CMOS microspeakers can monolithically integrate with control and driving integrated circuit. To enhance the output SPL, the MEMS electrostatic microspeaker is achieved by using relatively complicated processes [13]. There are several design concerns for the electrostatic microspeakers, for example, the requirement of high driving voltage, and the pull-in effect and limited SPL due to the initial gap between electrodes. In summary, to achieve enough SPL, especially

* Corresponding author at: Power Mechanical Engineering, National Tsing Hua Univ., Hsinchu, Taiwan.

E-mail address: fang@pme.nthu.edu.tw (W. Fang).

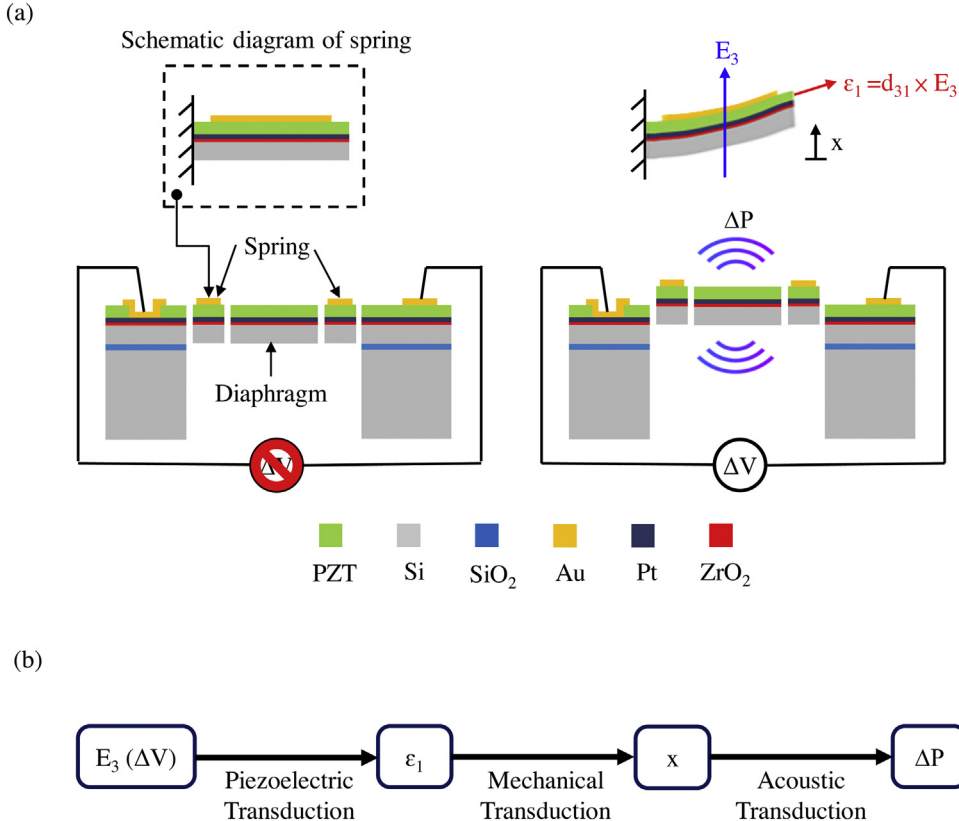


Fig. 1. The actuating mechanism of the proposed piezoelectric MEMS microspeaker: (a) the in-plane strain ε_1 in the PZT thin film caused by the out-of-plane input electric field E_3 will bend the springs and further lead the displacement x of the central diaphragm, and then the piston movement of the diaphragm will generate the pressure change ΔP , and (b) the design schema of the proposed piezoelectric MEMS microspeaker.

at low frequencies, with small volume by using the batch fabricated MEMS processes is the design issue for MEMS microspeakers.

The piezoelectric actuation is another approach to drive MEMS microspeakers. Various thin film piezoelectric materials such as the ZnO, AlN, and PZT have been employed for sensing and actuation applications. As reported in [14–18], the piezoelectric microspeakers which can be fabricated using the MEMS processes offer the advantages of large driving force, low power consumption, and single diaphragm structure. Thus, design concerns such as the pull-in effect and the traveling distance of the diaphragm are ignored. In recent years, the process technologies and material properties for piezoelectric thin films are continuously improved [19] which could further lead the performances enhancement of the piezoelectric microspeakers. The piezoelectric coefficient will affect the electromechanical conversion efficiency and further dominate the performance for actuation applications such as microspeakers. Typically, the PZT film has the highest d_{31} piezoelectric coefficient [20], and hence this study exploits the PZT thin film with a d_{31} piezoelectric coefficient of -40 pC/N as the actuation layer for microspeakers. The PZT thin film has also been applied to commercial MEMS microspeakers for earphones [5]. Although the size-reduction due to micromachining processes causes piezoelectric MEMS microspeakers much suitable for in-ear applications, the insufficient SPL at low frequencies is still a major concern. This study extends the designs in [21–22] to present the piezoelectric microspeaker design which consists of a diaphragm supported by flexible springs. Based on the proposed design of flexible springs and the driving electrodes for piezoelectric film, the SPL of microspeakers for in-ear applications can be enhanced. Measurements in the standard ear simulator demonstrate the feasibility of the presented designs. The frequency range for human communication voice is mainly 0.5 ~ 2 kHz [23], and the typical frequency range for hearing aids is below

5 kHz [24]. Hence, the target of present designs is to enhance the SPL at low frequencies, especially for communication voice range.

1.1. Design concepts and principles

The working principle of the proposed piezoelectric microspeaker is illustrated in Fig. 1. The microspeaker consists of a movable diaphragm and flexible springs formed by the Si and PZT bi-layer structure. The piezoelectric film on the springs has a top and a bottom driving electrodes. As shown in Fig. 1a, an in-plane strain ε_1 will be introduced on the PZT film when an out-of-plane electric field E_3 is applied on the top and bottom electrodes. The relation between the input electric field and the in-plane strain can be expressed as,

$$\varepsilon_1 = d_{31}E_3 \quad (1)$$

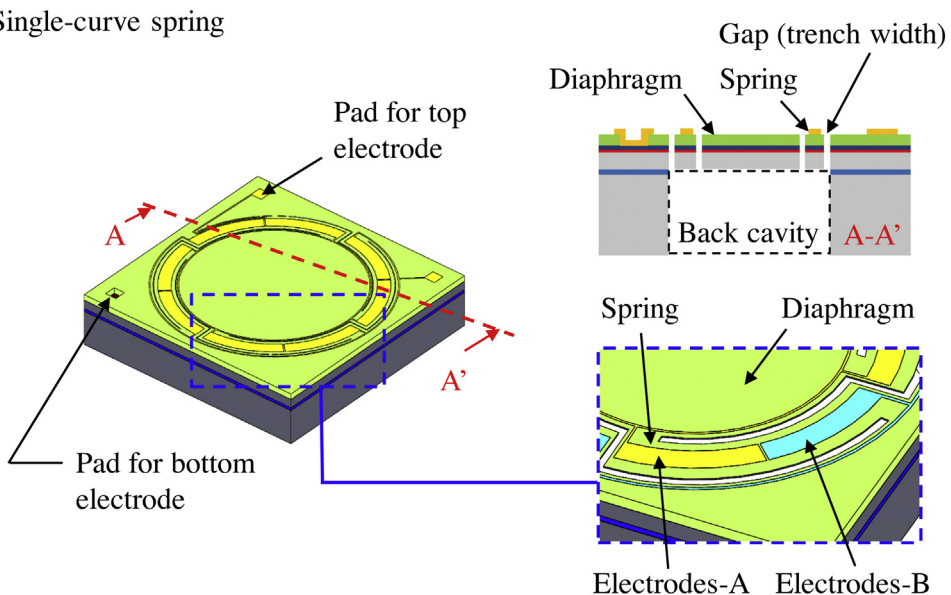
The in-plane strain in the PZT thin film will bend the springs formed by the PZT and Si bi-layers. The deformation of the springs will further lead to the piston motion of the central diaphragm, and the moving diaphragm will push the air to generate a pressure change ΔP . Fig. 1b summarizes the actuating schema of the piezoelectric MEMS microspeaker. For in-ear applications, ΔP can be expressed as [8], [10],

$$\Delta P = -\frac{1.4P_0}{V_0} \cdot \Delta V \quad (2)$$

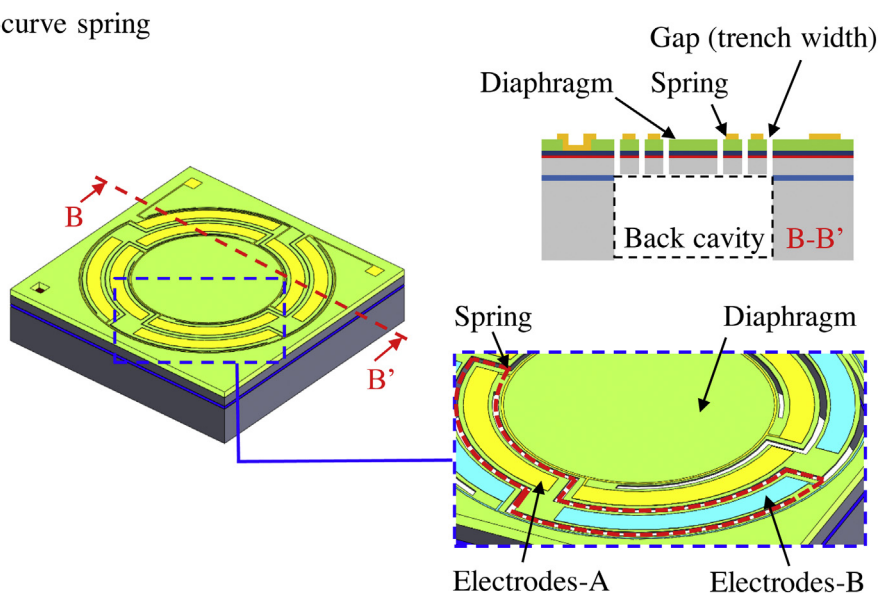
where P_0 is the ambient pressure, V_0 is the volume of the ear cavity, and ΔV is the displaced volume (volume change introduced by the piston-motion displacement x of diaphragm). Thus, the SPL L_{dB} can be determined as,

UUo different PZT microspeaker designs are proposed and also implemented on the SOI (silicon on insulator) wafer to show the

(a) Single-curve spring



(b) Dual-curve spring



(c) Clamped diaphragm

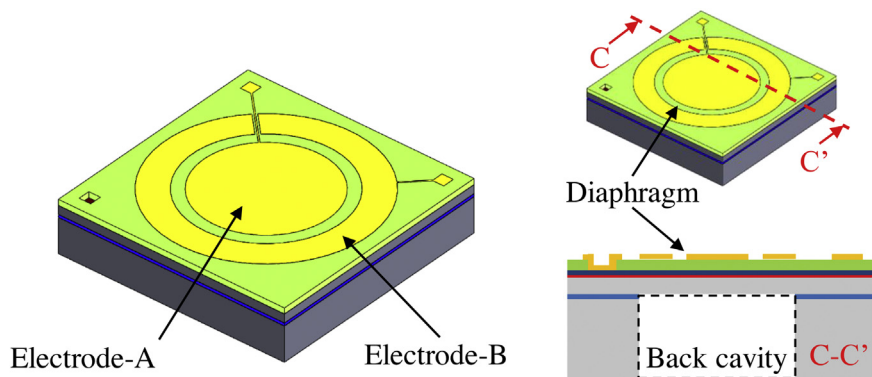


Fig. 2. The schematic illustrations of the piezoelectric MEMS microspeakers, (a) the proposed single-curve spring design, (b) the proposed dual-curve spring design, and (c) the reference clamped diaphragm.

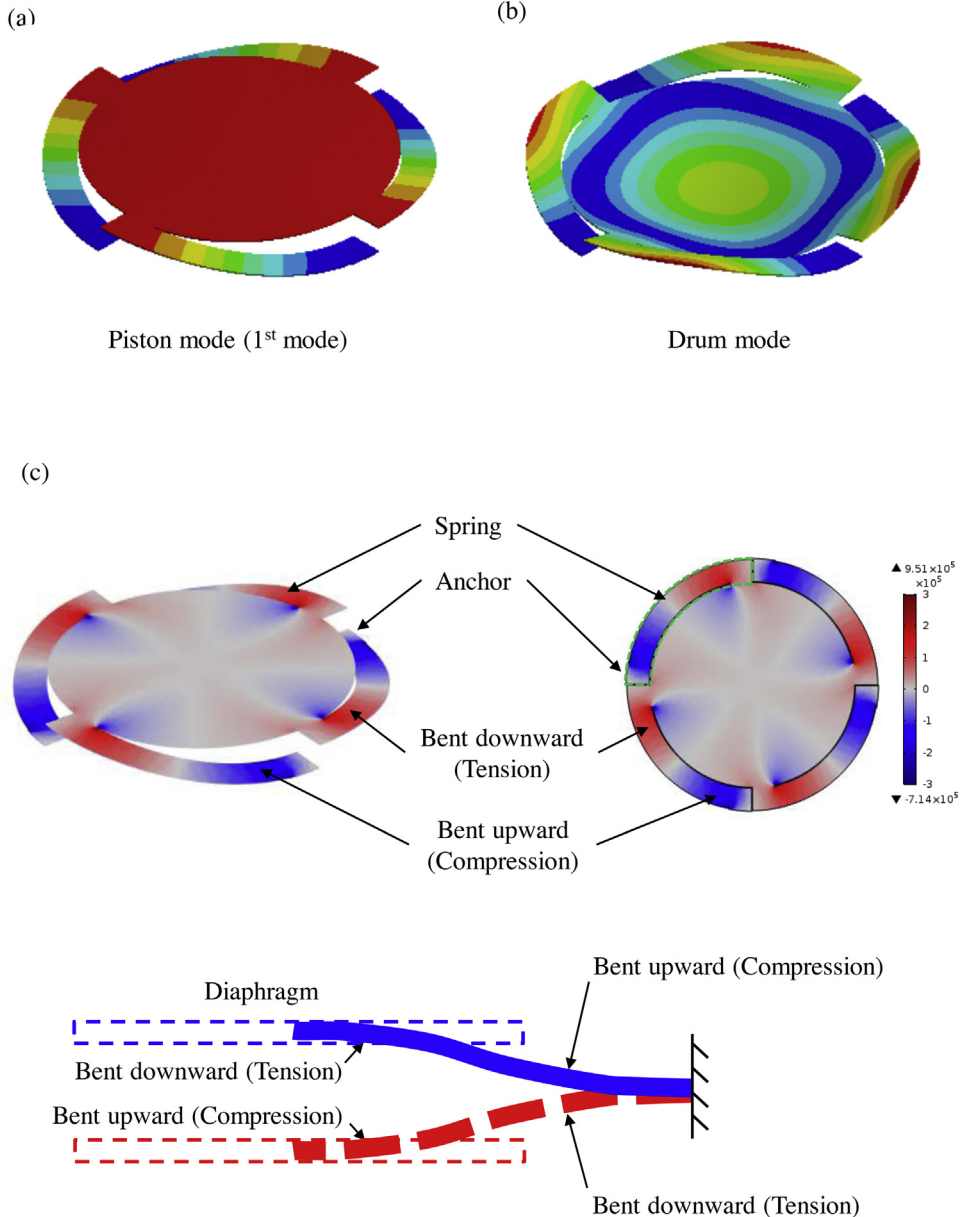


Fig. 3. The two vibration mode shapes of the microspeaker with single-curve spring design, (a) piston mode, (b) drum mode; and (c) the plane stress distribution of the single-curve spring structure when the microspeaker vibrating at its first mode.

performances enhancement by varying the design of structures and driving electrodes. Fig. 2a and b respectively illustrate the schematic view of two proposed microspeakers with different spring and diaphragm structures and the related driving electrodes designs. The reference clamped diaphragm microspeaker in Fig. 2c is also designed and implemented for comparison. The dual-electrode design is also applied to the clamped diaphragm microspeaker [25] to achieve its largest output for fair comparison. In the following sections, the design details of the proposed single-curve and dual-curve springs will be respectively presented. It should be noted that the dimensions of springs, electrodes and diaphragm have not been optimized.

1.2. Single-curve spring

The design of single-curve spring consists of a movable central diaphragm supported by four surrounded single-curve springs, as shown in Fig. 2a. There are gaps (named trench widths) between

the springs and central diaphragm. The diameter of back cavity is 1800 μm . The flexible springs are designed to enable much larger displacement of diaphragm to increase the pushed air volume and further improve the low-frequency SPL of microspeakers. The width of driving electrodes is designed as 100 μm to provide sufficient driving force. Thus, the width of the curve spring is designed as 160 μm to offer the space for electrical routings and process tolerance. Moreover, according to [26], the trench width below 10 μm could reduce the acoustic short circuit. In this study, the 5 μm trench width is selected to comply with process limitations. Thus, the diameter of central diaphragm is 1460 μm . The cross-section view depicts that both of the springs and diaphragm are consisted of the PZT film (1 μm thick) and the Si device layer (5 μm thick) of SOI wafer. Moreover, the handle layer of SOI wafer is 400 μm thick. The commercial finite element method (FEM) software (COMSOL and ANSYS) is employed to investigate the characteristics of the presented microspeaker. As the FEM simulation shown in Fig. 3a, the presented microspeaker has the piston vibration

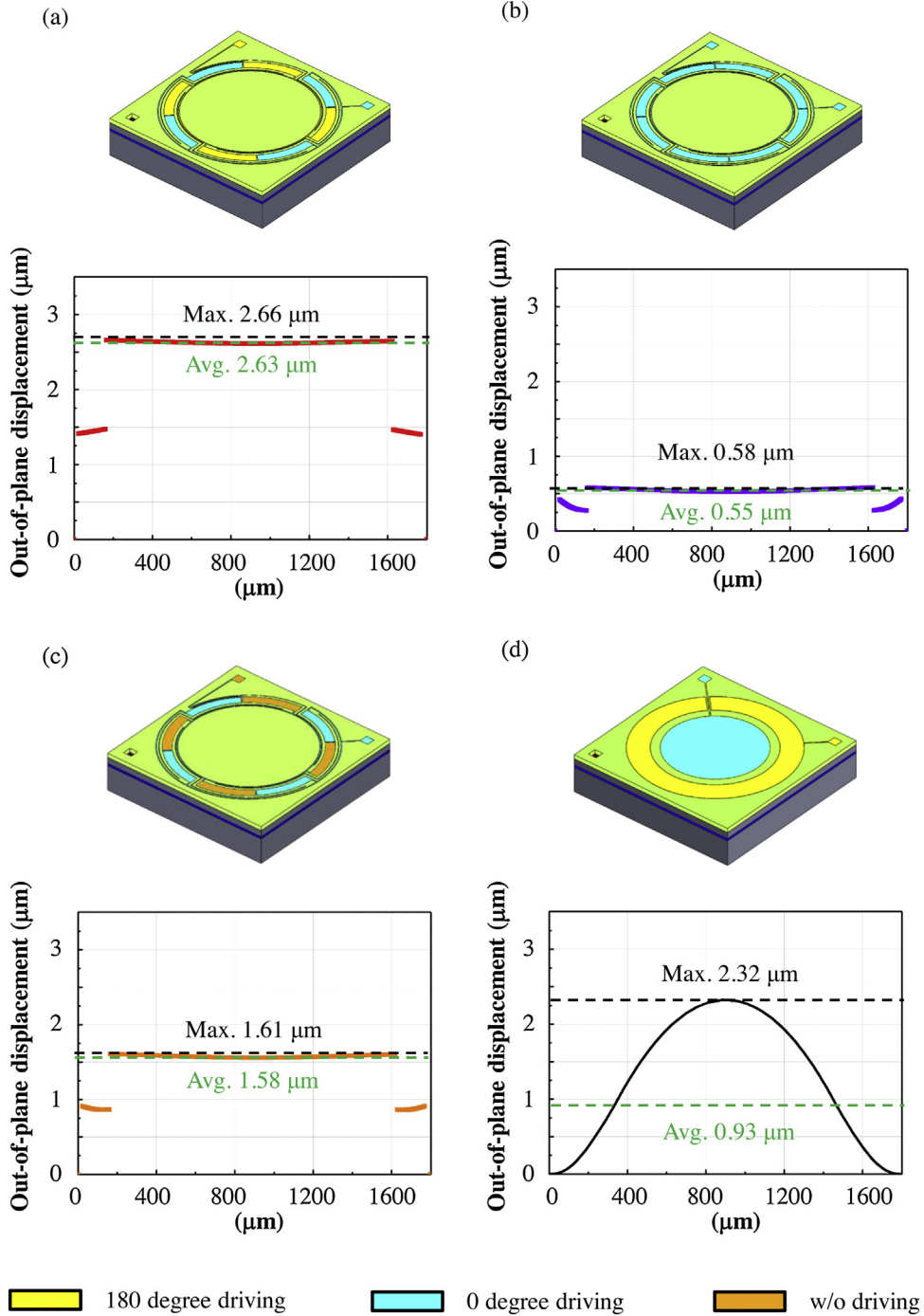


Fig. 4. The FEM simulated out-of-plane displacements of (a) the single-curve spring design with two electrodes (electrodes-A and electrodes-B) actuating out-of-phase, (b) the single-curve spring design with two electrodes (electrodes-A and electrodes-B) actuating in-phase, (c) the single-curve spring design with only one electrode (electrodes-B) actuating, and (d) the reference clamped diaphragm microspeaker with two electrodes actuating out-of-phase.

(diaphragm performing the up and down rigid body displacement while flexible springs having the bending deformations) as its first mode (3.1 kHz). The dimensions of spring-diaphragm structure is also designed to suppress other vibration modes within the audio range (20 Hz ~ 20 kHz), especially the drum mode shown in Fig. 3b. The resonant frequency of the drum mode which has a significant impact on the sound distortion [7] is designed as 22.4 kHz in this study. In addition, FEM simulation results in Fig. 3c further indicate the stress distribution of the microspeaker for its first vibration mode. The results show two opposite bending deformations (bent upward and downward, i.e. with the stress distribution

of compression-tension) on the springs. In other words, the PZT films should be designed to simultaneously offer two opposite actuations (expansion and shrinkage) on each spring to cause the required piston vibration of microspeaker to increase the output of microspeaker. As a result, two sets of actuating electrodes (electrodes-A in yellow and electrodes-B in blue, as indicated in Fig. 2a) are respectively arranged at different locations of springs and also driving separately (with different electrical routings).

This study employs the FEM simulation to predict and compare the performances of proposed and other microspeaker designs. Simulation results in Fig. 4a–b depict the out-of-plane displace-

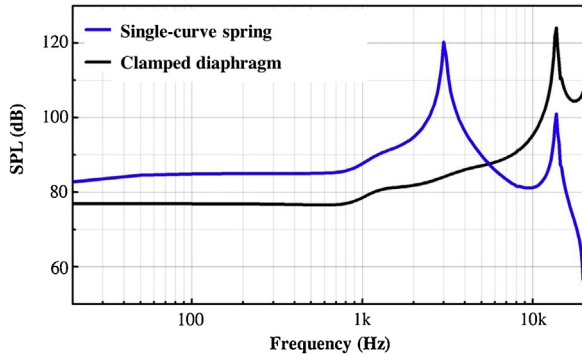


Fig. 5. Simulation results of the SPL for the proposed single-curve spring design and the reference clamped diaphragm microspeaker by using the COMSOL generic 711 coupler model.

ments of the diaphragm for the single-curve spring design with dual electrodes (electrodes-A and electrodes-B) actuating respectively out-of-phase and in-phase at 1 kHz, 2 V_{pp} (2 V_{pp} is selected based on the specification of many smart phones and consumer electronics). The average displacements depicted in figures are only determined from the central diaphragm. Since the central diaphragm of proposed design has almost no deformation during actuation, the maximum and average displacements are very close. In comparison, Fig. 4c shows the result when driven by only one electrode (electrodes-B) for the proposed design. The results indicate a larger output displacement is achieved when electrodes-A and electrodes-B driven at out-of-phase. Fig. 4d further demonstrates the comparison of out-of-plane displacement (driving with 1 kHz, 2 V_{pp} signal) between the single-curve spring design and the clamped diaphragm. The diameter of central top electrode of the clamped-diaphragm microspeaker is 1100 μm, and the width of the outer ring electrode is 240 μm. In this case, the average displacement is determined from the deformed clamped diaphragm. Since the clamped diaphragm vibrates in the drum mode during actuation, the displacements at the center and edge of diaphragm are very different. As a result, the average displacement is much lower than the maximum one. The FEM simulation results show the proposed single-curve spring design has larger maximum displacement and average displacement. The stress distribution of the single-curve spring structure driven at its resonant frequency of 3.1 kHz with 2 V_{pp} is also predicted by the FEM simulation. The structure has a maximum stress of 260 MPa at the connection of spring and its anchor. The maximum stress is much smaller than the yield strength of Si (near 7.0 GPa in [27]), hence the damage of structure is ignored when microspeaker is driven at 2 V_{pp}. In addition, as displayed in Fig. 4, the sound waves produced by the piston mode of the proposed spring-supported diaphragm have better quality from the acoustic point of view (compared with those generated by the drum mode of typical fully-clamped diaphragm) [7]. Then, to verify the design concept of the single-curve spring design (with dual electrodes driven at out-of-phase), the output SPL in an ear simulator is predicted by the COMSOL generic 711 coupler model, as shown in Fig. 5. According to the results, the proposed single-curve spring design improves the low-frequency (< 5.5 kHz) SPL compared with the typical clamped diaphragm. However, the proposed design sacrifices part of the diaphragm area to realize the spring structure. Moreover, the reference design with clamped diaphragm has its first resonant frequency near 20 kHz. Thus, the proposed design has lower SPL than the reference type at high frequencies (> 5.5 kHz). In addition, the slightly SPL decrease at low frequencies of the proposed design is caused by the 5 μm gaps (trench width) between the springs and the central diaphragm. Note that the peaks around

14 kHz in Fig. 5 are the typical response caused by the ear simulator.

1.3. Dual-curve spring

To further enhance the SPL at low frequencies, the dual-curve spring with a lower stiffness structure is also proposed and investigated in this study. With the same form factor (including springs and diaphragm) compared with the single-curve spring, a longer suspended structure is realized by the proposed dual-curve geometry design shown in Fig. 2b. The widths of driving electrodes, curve springs, and trenches are the same as those of the single-curve spring microspeaker. To keep the same footprint of microspeakers for fair comparison, the diameter of central diaphragm for dual-curve spring design becomes 1130 μm. Due to the lower stiffness of dual-curve springs, the larger output displacement of the central diaphragm is expected. The 1 μm PZT and 5 μm Si are selected as the structure thickness for the design of dual-curve spring as well. With the 5 μm thick Si device layer and the smaller diameter of central diaphragm compared with single-curve spring design, the resonant frequency of drum mode of the dual-curve spring design (35.1 kHz) is even farther from the audio range. Similarly, for the design of driving electrodes, the FEM simulation is employed to investigate the stress distribution on the spring during the actuation of microspeaker. The FEM simulation results in Fig. 6 depict the stress distribution on two dual-curve spring designs when microspeaker driving at the first vibration mode. As depicted by the colors in Fig. 6a, the proposed dual-curve spring design has two opposite bending deformations (bent upward and downward) along the spring structure, and its resonant frequency is 1.7 kHz. In comparison, as displayed by the colors in Fig. 6b, the folded spring (also dual-curve) widely used in MEMS devices [28] has four opposite bending deformations (bent upward-downward-upward-downward, i.e. with the stress distribution of compression-tension-compression-tension) along the spring structure during the actuation of microspeaker. In other words, for the proposed design, the PZT films will simultaneously offer two opposite actuations (expansion and shrinkage) on the dual-curve springs to cause the required piston vibration of microspeaker. As displayed in Fig. 2b, two sets of actuating electrodes (electrodes-A in yellow and electrodes-B in blue) and their electrical routings are respectively arranged on the dual-curve springs. However, for the folded-spring counterpart in Fig. 6b, four sets of driving electrodes and their relatively complicated electrical routings are needed to fulfill the requirement of actuation.

The FEM simulation of single- and dual-electrode driving was also performed to verify the feasibility of applying dual-electrode design on the dual-curve springs. As presented in Fig. 7a-c, actuating with dual electrodes, the larger out-of-plane displacement is predicted. Then, the FEM simulation results in Fig. 7d depicts that the diaphragm of proposed type has much larger maximum and average out-of-plane displacement (driving at 1 kHz, 2 V_{pp}), compared with the typical clamped diaphragm. Furthermore, the dual-curve spring design offers the piston movement of the central diaphragm, so the better sound quality is also achieved. The stress distribution of the dual-curve spring structure driven at its resonant frequency of 1.7 kHz with 2 V_{pp} has also been investigated. The structure has a maximum stress of 110 MPa at the connection of spring and its anchor. The maximum stress is also much smaller than the yield strength of Si. The SPL simulation in the COMSOL generic 711 coupler model was conducted as well. The frequency responses in Fig. 8 demonstrate the proposed dual-curve spring design not only achieves a significant improvement at low frequencies (< 4 kHz) over the typical clamped diaphragm, but also further enhance the low-frequency SPL compared with the single-curve spring design (Fig. 5). Besides, the trench width of 5 μm is also

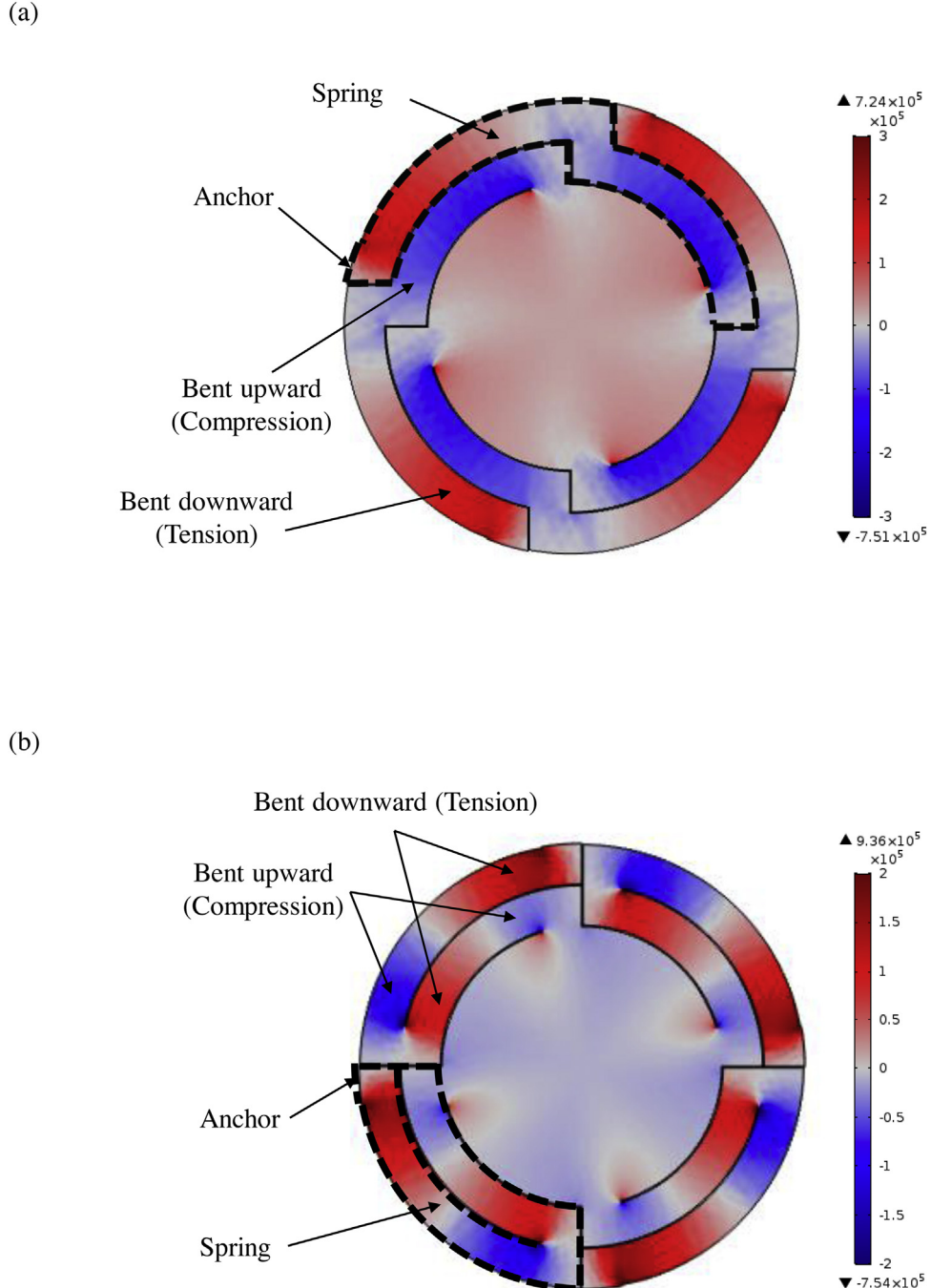


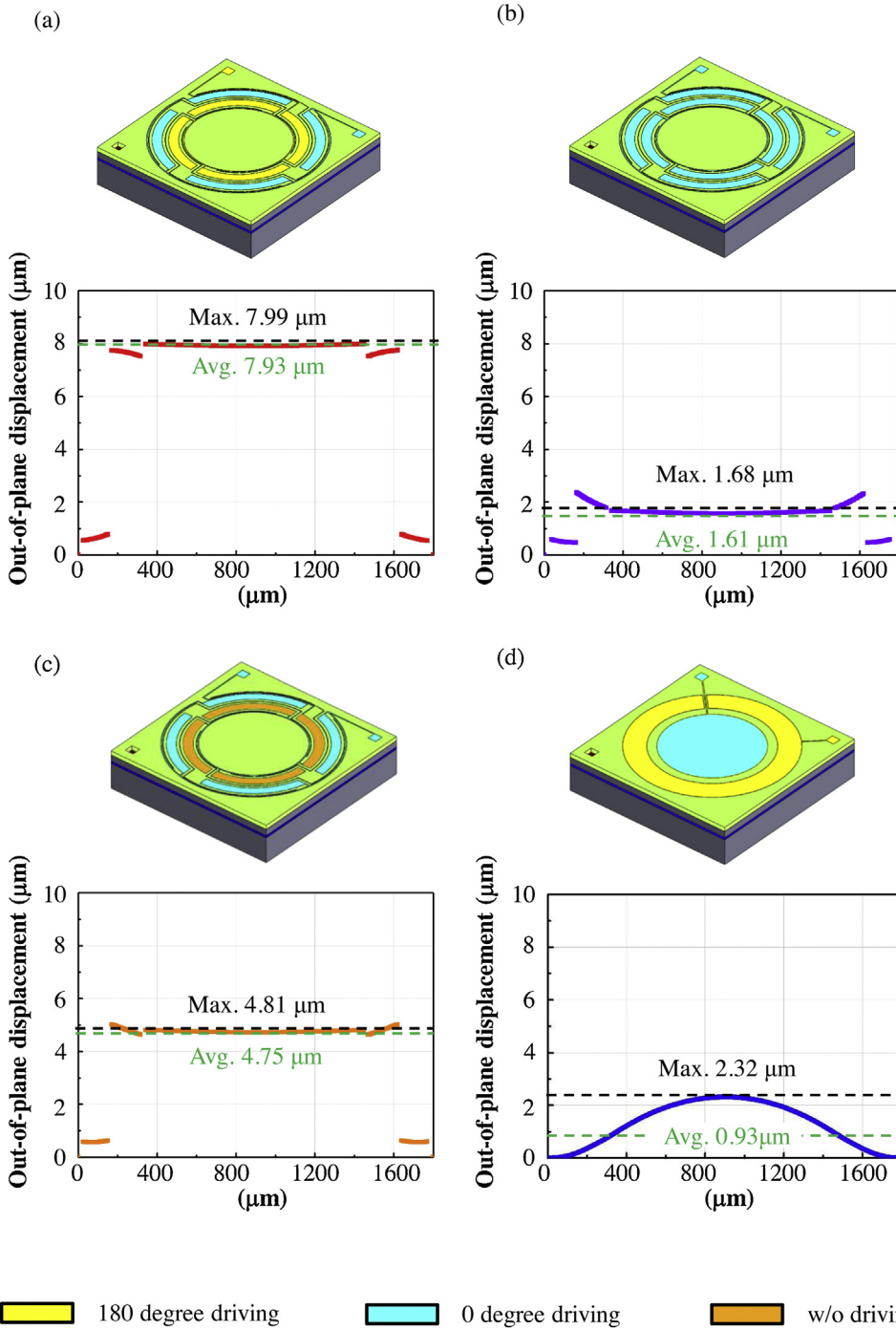
Fig. 6. The FEM simulated plane stress distribution of the dual-curve spring structures when the microspeaker vibrating at its first mode, (a) the proposed dual-curve spring has simple bending profile (stress distribution): bent upward (compression) – bent downward (tension), (b) the reference folded spring has complicated bending profile (stress distribution): bent upward (compression) – bent downward (tension) – bent upward (compression) – bent downward (tension).

designed to minimize the SPL drop at low frequencies. However, the lower SPL of the dual-curve spring design at high frequencies due to the smaller diaphragm area is observed as well.

2. Fabrication and results

This study employs the fabrication processes in Fig. 9 to implement the presented microspeakers. First, as shown in Fig. 9a, the ZrO_2 (15 nm thick) and Pt (150 nm thick) thin films were deposited on the Si device layer (5 μm thick) of SOI wafer to form the bottom electrode layer. The ZrO_2 was served as the adhesion layer for Pt, and also the insulation layer to avoid generating leakage current.

After that, a 1 μm thick PZT film was deposited by the sputtering process. Then, as depicted in Fig. 9b, the PZT film was patterned by wet etching to expose bond pads of bottom electrode. As illustrated in Fig. 9c, the Cr (20 nm thick) and Au (200 nm thick) thin films were then deposited and patterned to serve as the top electrode and electrical routings. As displayed in Fig. 9d, trenches on PZT film and Si device layer were realized by the front side ICP etching to define the springs and diaphragm structures. During the ICP etching process, both PZT and Pt films were etched by the mixed gas of Ar (40 sccm) and CF_4 (70 sccm) with the chamber pressure fixed at 1 Pa. Moreover, the RF power was selected as 800 W with a bias voltage of 200 V. Note that after the PZT layer was removed, there were some



■ 180 degree driving ■ 0 degree driving ■ w/o driving

Fig. 7. The FEM simulated out-of-plane displacements of (a) the dual-curve spring design with two electrodes (electrodes-A and electrodes-B) actuating out-of-phase, (b) the dual-curve spring design with two electrodes (electrodes-A and electrodes-B) actuating in-phase, (c) the dual-curve spring design with only one electrode (electrodes-B) actuating, and (d) the reference clamped diaphragm microspeaker with two electrodes actuating out-of-phase.

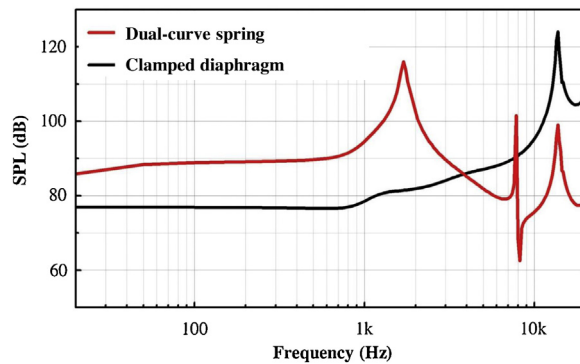


Fig. 8. Simulation results of the SPL for the proposed dual-curve spring design and the reference clamped diaphragm microspeaker by using the COMSOL generic 711 coupler model.

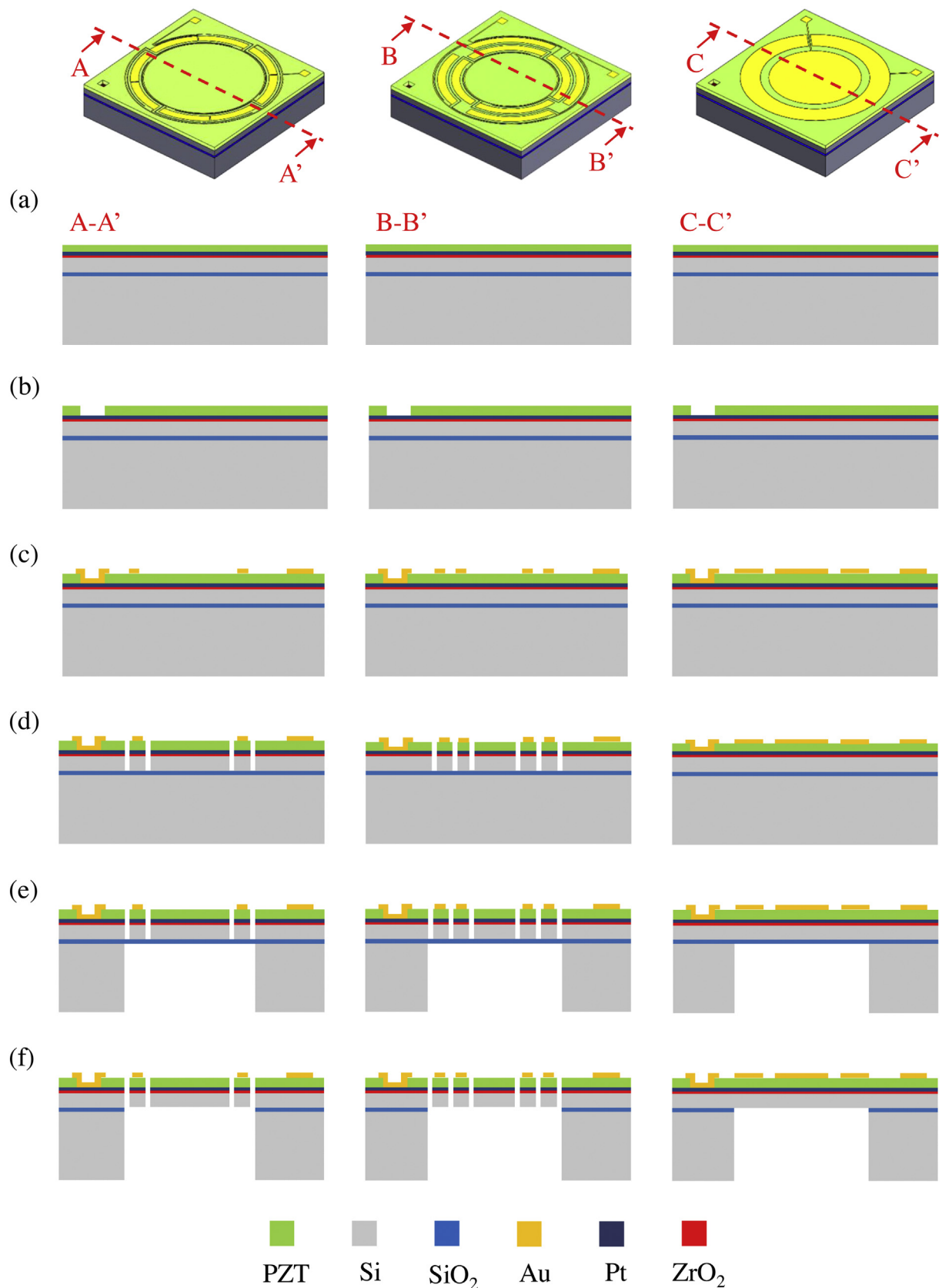


Fig. 9. Fabrication processes for the devices, (a) deposition of ZrO₂ insulation layer, Pt bottom electrode, and PZT piezoelectric layer, (b) PZT wet etching to define the bonding pads for bottom electrode, (c) patterning the top electrodes by E-gun deposition and lift-off process, (d) front-side dry etching to define the spring-diaphragm structure, (e) back-side DRIE to define the back cavities of microspeakers, and (f) back-side RIE to release the movable structures.

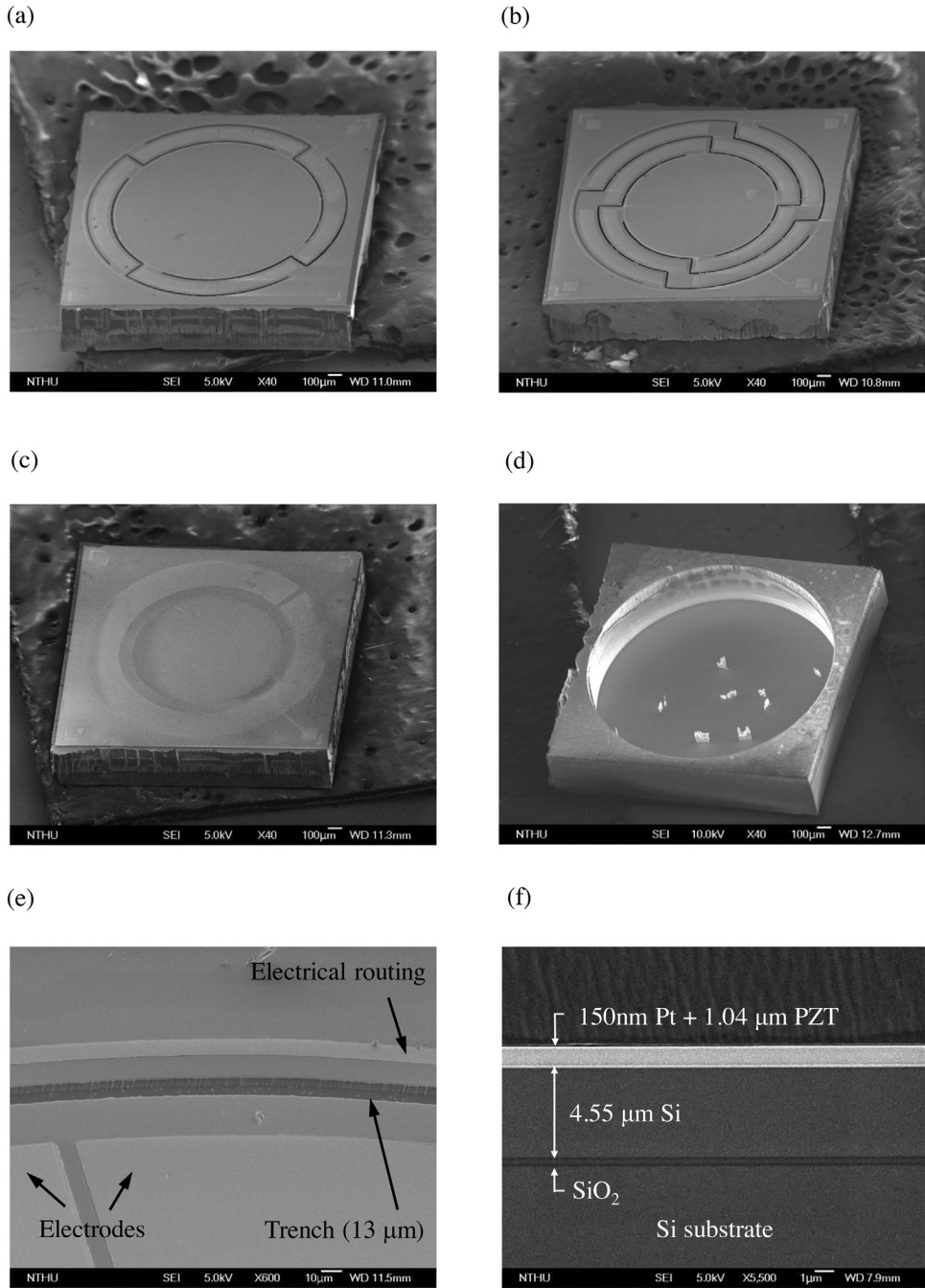


Fig. 10. The SEM micrographs of typical fabricated devices, (a) the proposed single-curve spring design, (b) the proposed dual-curve spring design, (c) the reference clamped diaphragm microspeaker, (d) the back cavity of the microspeaker, (e) the trench defined by the DRIE and dual electrodes and the electrical routing patterned by the lift-off process, and (f) cross-section of the substrate to show the PZT and Pt thin films deposited on the SOI wafer.

remaining PZT particles on Pt layer, which would affect the following etching process. Hence, the wafer was dipped in the solution with 1% NaF and 10% HCl to remove the particles before the etching of Pt film. After patterned the PZT and Pt films, the front-side trenches were defined on Si device layer by ICP etching. As depicted in Fig. 9e-f, the handle Si substrate was etched by DRIE to define the back cavity of microspeaker, and after that the RIE was employed to remove the buried oxide of SOI wafer to release the springs and diaphragms of microspeakers.

Micrographs in Fig. 10 display typical fabricated piezoelectric MEMS microspeakers. The micrographs in Figs. 10a-b respectively demonstrate the MEMS microspeakers with the single-curve

and the dual-curve springs. Fig. 10c further depicts the reference type microspeaker with clamped diaphragm design. As shown in Fig. 10d, the micrograph from the back-side of substrate displays the back cavity defined by the DRIE and the fully clamped diaphragm. The zoom-in micrograph in Fig. 10e shows the electrodes on the spring, and the electrical routing on the substrate. A near 13 µm trench between the suspended spring and the substrate is also observed. The cross-section view in Fig. 10f further displays the bi-layer structure consisted of the PZT film and the Si device layer. Besides, the Si substrate and the buried oxide layer of SOI wafer and the Pt bottom electrode can also be observed. Fig. 11a illustrates the cross section of the device-under-test (DUT) with

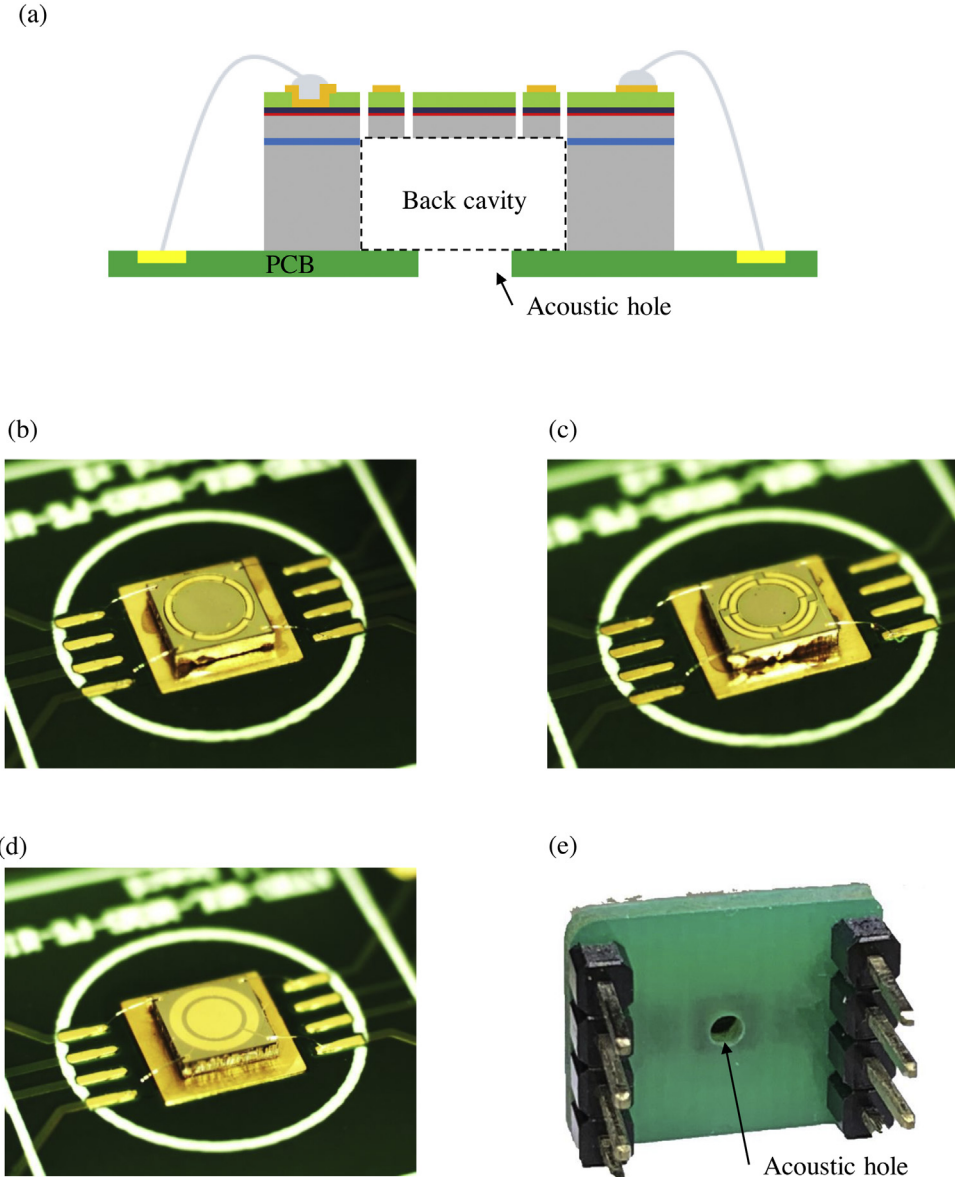


Fig. 11. The microspeaker chip wire-bonding on PCB with an acoustic hole as the DUT, (a) the schematic illustration, and micrographs of DUT for (b) the single-curve spring microspeaker chip, (c) the dual-curve spring microspeaker chip, (d) the clamped diaphragm microspeaker chip, and (e) the backside acoustic hole.

a microspeaker chip wire bonded and mounted on a printed circuit board (PCB) with an acoustic hole for the characterization of acoustic performances. Note that with the existing of acoustic hole on the PCB, the volume of microspeaker back chamber will not be limited by the size of back cavity on chip. Hence, the influence of back chamber on the resonant frequency of microspeaker could be minimized during measurements [29]. Micrographs in Fig. 11b-d display the DUT of three different microspeaker designs. Micrograph in Fig. 11e shows the acoustic hole on the PCB at the back side of DUT.

3. Measurement and results

To evaluate the characteristics of the PZT thin film and the performance of the proposed MEMS microspeakers, various experiments have been conducted in this study. In the following sub-sections, the measurement results of piezoelectric properties and acoustic performance are reported and discussed.

3.1. Piezoelectric properties of the PZT thin film

Firstly, this study employs the dynamic measurement approach in [30] to evaluate the critical material property of piezoelectric coefficient d_{31} . The bi-layer (consisted of PZT film and Si device layer) cantilever test keys with three different dimensions (width: 50 μm , length: 250 μm , 300 μm , 400 μm) were fabricated to characterize the piezoelectric coefficient d_{31} . As depicted in Fig. 12a, the natural frequencies and dynamic displacements of the test keys were measured by the Laser Doppler Vibrometer (LDV). Thus, the static displacement δ_{st} is determined by,

$$\frac{\delta_{dy}}{\delta_{st}} = \frac{1}{\sqrt{\left(1 - \left(\frac{\omega_{input}}{\omega_n}\right)^2\right)^2 + \left(2\xi\frac{\omega_{input}}{\omega_n}\right)^2}} \quad (4)$$

in which δ_{dy} is the dynamic displacement, ω_{input} is the driving frequency, ω_n is the natural frequency of the cantilever, and ξ is the

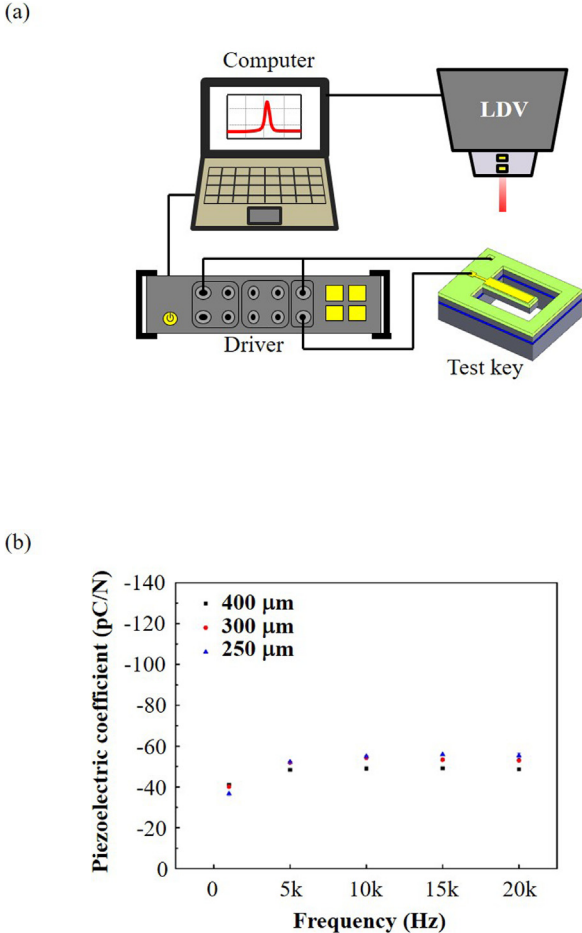


Fig. 12. (a) The dynamic measurement setup to determine the piezoelectric coefficient, (b) the d_{31} coefficient determined by the dynamic measurement from test cantilevers of three different lengths.

damping ratio (ξ can be determined from the LDV measurement results). Subsequently, the d_{31} coefficient can be extracted from,

$$\delta_{st} = \frac{3d_{31}s_s s_p t_s (t_s + t_p) L^2 V}{s_s^2 t_p^4 + 4s_s s_p t_s t_p^3 + 6s_s s_p t_s^2 t_p^2 + 4s_s s_p t_s^3 t_p + s_p^2 t_s^4} \quad (5)$$

where, s_s and s_p are the mechanical compliances of the Si device layer and the PZT thin film, t_s and t_p are the thickness of the Si and PZT, L is the length of the cantilever, and V is the driving voltage. Fig. 12b shows the d_{31} coefficients extracted from dynamic responses of different driving frequencies. According to Eq. (4), the resonant effect on the measurement results in [31] will be canceled out. Thus, the d_{31} coefficients show similar levels over various driving frequencies. In this study, the d_{31} coefficient of the PZT thin film is around -45 pC/N.

3.2. Preliminary tests in the acrylic tube

The acoustic performance evaluation was conducted in the anechoic box. Fig. 13a shows the whole measurement setup. As displayed in Fig. 13b, to simulate in-ear applications, the DUT shown in Fig. 11 was mounted in the acrylic baffle connecting to the acrylic tube, and the standard microphone (G.R.A.S. 46BE) was fixed on the other side of the tube. The chamber of the tube between the DUT and the standard microphone is 30 mm long with 1.3 cm^3 in volume. Actuated by the signals from the B&K pulse spectrum analyzer, the DUT produced the sound waves that would pass through the chamber of the tube. After the sound pressure was received

by the standard microphone, the data would be transmitted to the B&K pulse spectrum analyzer and then recorded by the computer.

Measurements results in Fig. 14 demonstrate the preliminary test results of the two proposed (diaphragm supported by single-curve and dual-curve springs) and the reference (fully clamped diaphragm) microspeakers. The results in Fig. 14a-b respectively depict the SPL of microspeakers with single-curve and dual-curve spring designs. The two curves in each figure show the difference between the single- (electrodes-B) and dual-electrode (electrodes-A&B) driving. Fig. 14c further shows the SPL difference of the reference design. By the dual-electrode driving (2 V_{pp}), the SPL of these three designs can increase 3~6 dB in most of the frequencies compared with the single-electrode driving. The results verify the design concept of dual electrodes. In addition, with dual-electrode driving, the highest SPL of the single- and dual-curve spring designs can reach 88.7 dB and 90.1 dB respectively. It is worthy to note that the peaks around 6, 12, and 18 kHz in all the frequency responses are not caused by the resonance of the structures but caused by the standing waves of the tube. Fig. 14d shows the comparison of SPL (driving with dual-electrodes) among the above three microspeakers investigated in this study. Driving with dual electrodes at 2 V_{pp}, the SPL of the single-curve spring design is 25 dB higher than reference type (clamped diaphragm) at 3.2 kHz and is more than 6 dB higher in most of the human voice frequency range from 20 Hz to 5 kHz. As for the dual-curve spring design, the SPL is 29.1 dB higher than the reference type at 1.85 kHz and at the relative low-frequency range from 20 Hz to 3.8 kHz, a significant SPL improvement over the reference design is achieved by the dual-curve spring design. Besides, as compared with the single-curve spring design, the dual-curve spring one demonstrates a further SPL enhancement at low frequencies from 100 Hz to 2.3 kHz. It confirms the design concept of the dual-curve springs. It should be noted that because of the longer trenches, which is essential for a longer spring design, the low-frequency SPL of the dual-curve spring design drops faster and becomes lower than the single-curve spring design below 100 Hz. Also, the lower SPL at high frequencies is owing to the sacrifice of diaphragm area to realize the longer springs.

Table 1 summarizes the results of the preliminary tests. It can be seen that by combining the springs and dual-electrode design, the performances of the two proposed designs at low frequencies have a remarkable enhancement compared with the typical clamped-diaphragm design. Moreover, the dual-curve spring design shows the highest SPL at 1 kHz. In consideration of the major challenge: low-frequency SPL for current MEMS microspeakers, the dual-curve spring design will be a better solution. As a consequence, further experiments using the standard ear simulator system was conducted to evaluate the acoustic performance of the dual-curve spring design.

3.3. Acoustic performance in the ear simulator system

To further establish reliable measurement data, the standard ear simulator system G.R.A.S. 43AG-6 was utilized in this study. The measurement setup is displayed in Fig. 15a. The DUT was assembled in the customized acrylic adapter, which was fixed on the external ear canal (G.R.A.S. GR0408) connecting to the ear simulator (G.R.A.S. RA0401). The photos in Fig. 15b show the commercial ear simulator, adapter, DUT, and other related setup for testing. As the DUT was driven by the B&K pulse spectrum analyzer to generate the sound pressure, the signal would be received by the microphone (G.R.A.S. 40AG) and then transmitted through the power module (G.R.A.S. 12AR) to the B&K pulse spectrum analyzer. Finally, the results were recorded by the computer.

Fig. 16 depicts the acoustic measurement results of the proposed dual-curve spring design and the reference clamped diaphragm.

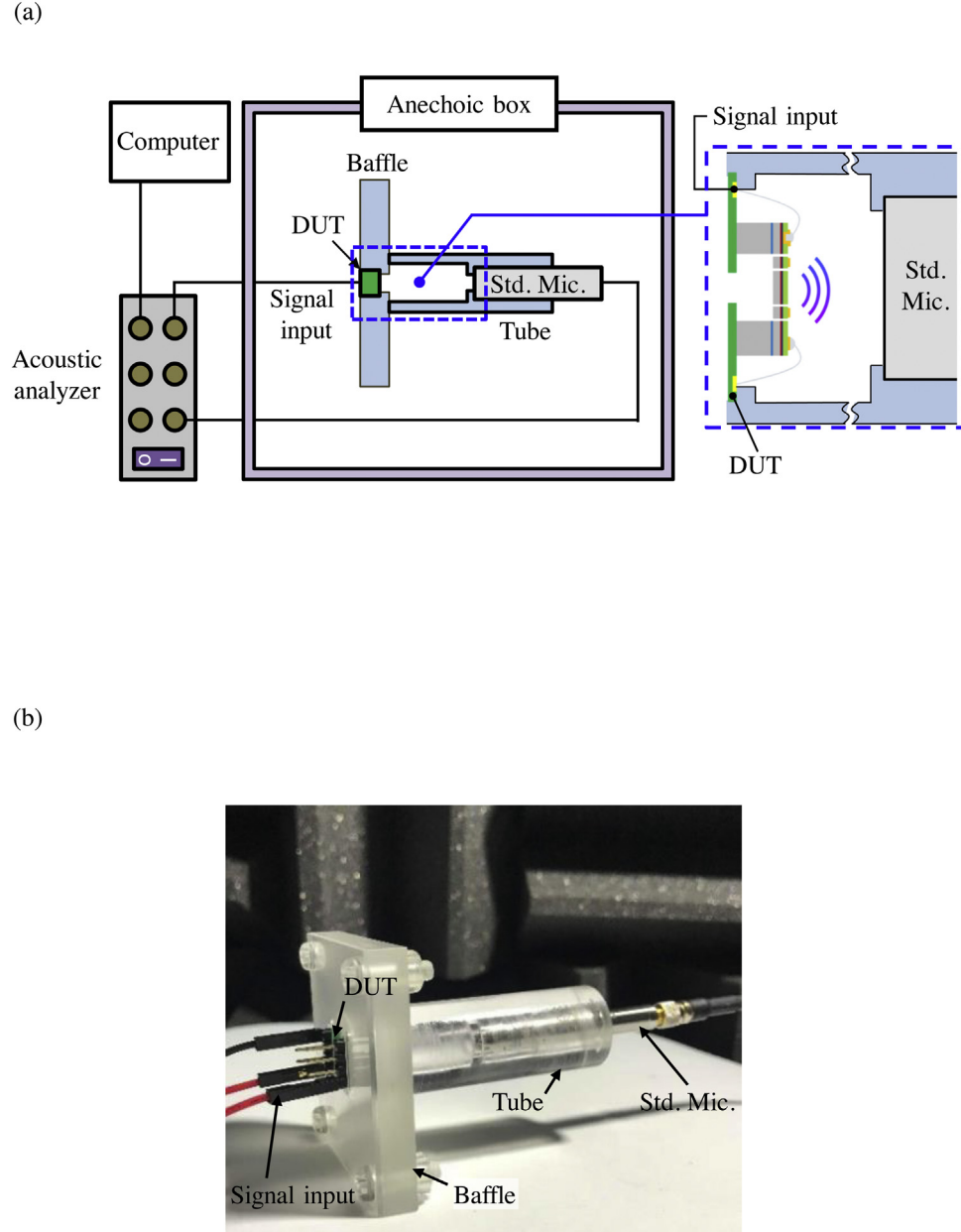


Fig. 13. (a) The schematic illustration of the test setup for the preliminary acoustic measurements, and (b) the photograph to show the acrylic tube and baffle to mount the DUT and the microphone.

Table 2

The comparison of the proposed, the reference, and the existing MEMS piezoelectric MEMS microspeakers.

Design	Clamped diaphragm	Dual-curve spring	F. Stoppel [18]	Unit
Diaphragm area	2.54	1	16	mm ²
Measuring distance	^a 35	^a 35	^a	mm
Driving voltage	2	2	2	V _{pp}
SPL at 1 kHz	56.4	74.5	86	dB
Normalized SPL at 1 kHz	48.3	74.5	61.9	dB

^a In the ear simulator G.R.A.S RA0401.

The frequency responses in Fig. 16a–b respectively show the SPLs of proposed (dual-curve spring) and reference designs after driven by single and dual electrodes (2 V_{pp}). Once again, the results verify driving with dual electrodes can further increase the SPL of the microspeakers. The highest SPL of the dual-curve spring design

can reach 87.1 dB. The peaks around 6, 12, and 18 kHz caused by Helmholtz resonance of the external ear canal can be observed in Fig. 16a–b as well. Moreover, it is worthy to note that in Fig. 16a, the much lower SPL produced by the electrodes-A is caused by the stress distribution during out-of-plane motion. Near the anchors

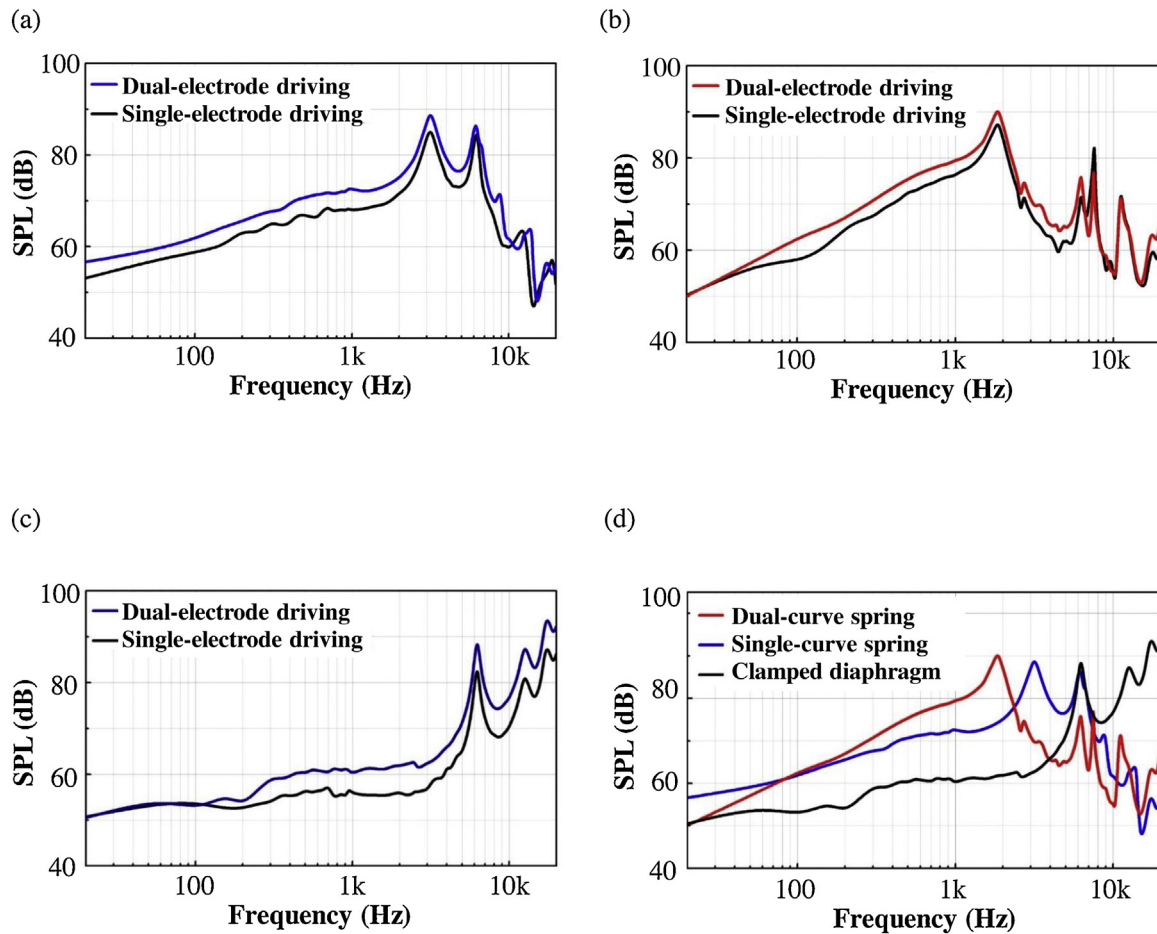


Fig. 14. Measured frequency responses of SPL (preliminary tests in the acrylic tube) for the three different microspeakers driven by dual electrodes (electrodes-A and electrodes-B) and single electrode (electrodes-B), (a) the proposed single-curve spring design, (b) the proposed dual-curve spring design, (c) the reference clamped diaphragm microspeaker, and (d) the comparison of the above three SPL frequency responses with dual-electrode driving.

Table 1

Specs and measurement results (from preliminary tests in the acrylic tube) to compare the performances of proposed and reference microspeakers.

Design	Clamped diaphragm	Single-curve spring	Dual-curve spring	Unit
Diaphragm area	2.54	1.67	1	mm ²
Measuring distance	^a 30	^a 30	^a 30	mm
Driving voltage	2	2	2	V _{pp}
SPL at 1 kHz	61.5	72.6	79.5	dB
Maximum SPL (Resonant frequency)	98.9 (20.0)	88.7 (3.2)	90.1 (1.85)	dB (kHz)

^a In the acrylic tube.

of the dual-curve springs, the area of electrodes-B has larger stress than the electrodes-A. According to the inverse piezoelectric effect, the larger average plane stress in the same electrode area, the higher the output sound pressure. Fig. 16c shows the comparison between the proposed and the reference designs. When driving at 2 V_{pp}, the dual-curve spring design is 28 dB SPL higher than the clamped diaphragm at the resonant frequency of 1.85 kHz. In addition, the proposed design demonstrates a significant enhancement over the reference type at low frequencies (< 3.5 kHz). From 100 Hz to 3 kHz, more than 10 dB SPL increase is achieved. Besides, Fig. 16c also depicts the low-frequency SPL loss caused by the trenches between the springs and the central diaphragm. Due to the expansion of the trenches during the dry etching process, the dual-curve spring design suffers more server SPL loss at low frequencies than the expectation of the FEM simulation. Compared with the clamped diaphragm design, the sharper drop of SPL of the dual-curve spring design at low frequencies can be clearly observed. To evaluate the

sound quality of the microspeakers, the THD measurement is also conducted (at 2 V_{pp}). As depicted in Fig. 16d, the THD of the dual-curve spring design is less than 2% in most of the audio range and is lower than 8% even at the peaks of resonant frequency or harmonic frequencies. The overall THD of the dual-curve spring design is lower than the clamped diaphragm. These results indicate the better sound quality can be achieved by the proposed dual-curve spring design.

Table 2 sums up the measurement results in the ear simulator and compares the results with existing piezoelectric MEMS microspeakers. Consistent with the conclusions in the preliminary tests, the dual-curve spring design shows the better performance at low frequencies. Furthermore, with the smallest diaphragm of 1 mm², the proposed design still shows a reasonable SPL with low input voltage of 2 V_{pp}, which will be compatible with consumer products. If the SPL is normalized to the diaphragm area, the dual-curve spring design even demonstrates the highest SPL at 1 kHz.

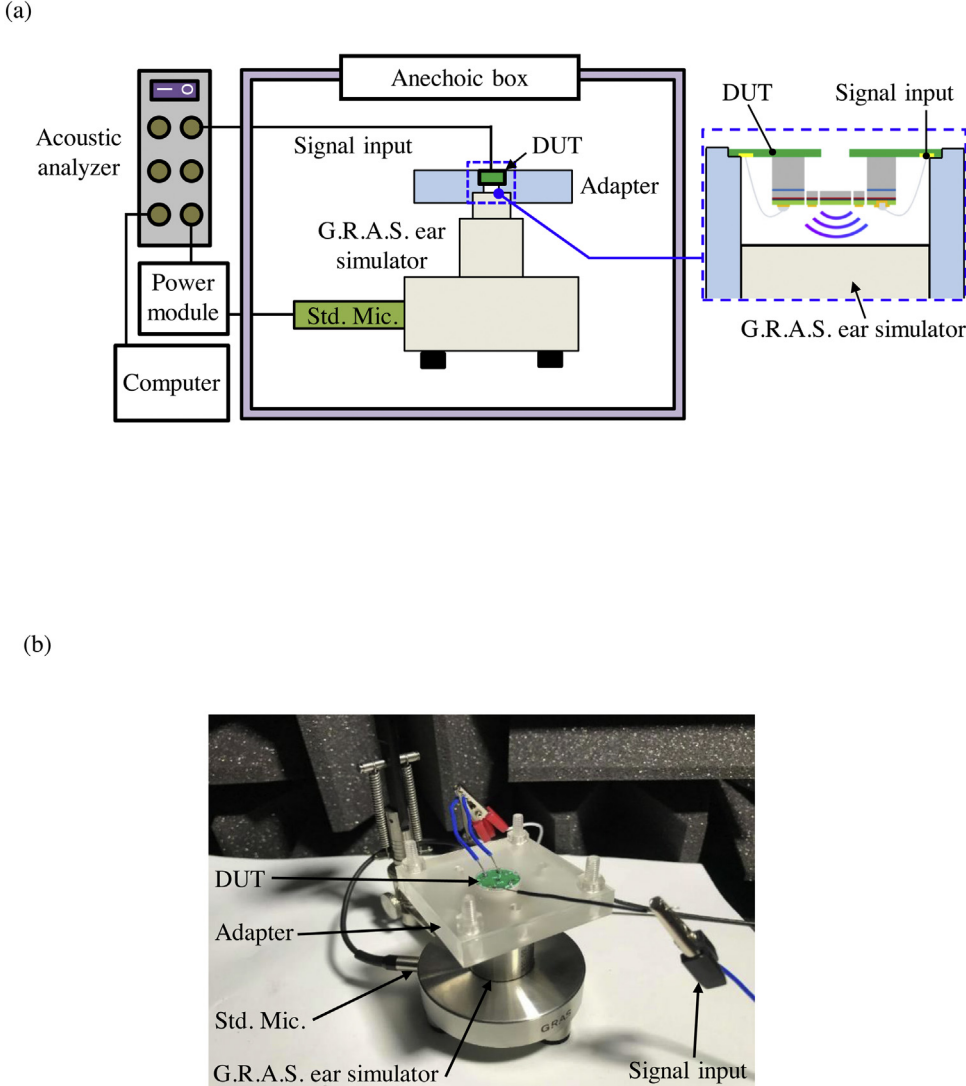


Fig. 15. (a) The schematic illustration of the test setup for the ear simulator system, and (b) the photograph to show the commercial ear simulator, adapter, DUT, and other related setup for testing.

4. Conclusions

The piezoelectric actuation has the potential to be a promising driving approach for the MEMS microspeaker. Presently, investigations to enhance the performances of piezoelectric microspeaker include the design of actuation material, structure, driving electrode, and so on. This study presents two structure designs together with the driving electrodes to improve the SPL of piezoelectric MEMS microspeakers at low frequencies. Unlike the existing fully clamped diaphragm microspeaker, this study exploits flexible springs, including the single-curve spring and dual-curve spring designs, to support the diaphragm. To enlarge the output displacement of the diaphragm to achieve a larger SPL, the dual electrodes are designed to drive the springs. To demonstrate the present concept, the proposed microspeakers were realized on the SOI wafer with 5 μm thick Si device layer, on which 1 μm thick PZT thin film was deposited as actuating material. Preliminary test results reveal that both single-curve spring and dual-curve spring designs achieve significant enhancement over the clamped diaphragm microspeaker at low frequencies. Measurement results in the standard ear simulator system further show the SPL of dual-curve spring design is 28 dB higher than the clamped diaphragm

at the 1.85 kHz, and display more than 10 dB improvement over the clamped type from 100 Hz to 3 kHz. In most of the audio range, the THD of dual-curve spring design (less than 2%) is lower than that of the clamped diaphragm as well. With low input voltage of 2 V_{pp} and the smallest diaphragm area of 1 mm^2 , the proposed dual-curve spring design still shows a reasonable SPL compared with the published literature. It is possible to further increase the SPL by increasing the input voltage. However, the bipolar fatigue of PZT thin film is the concern when increasing the driving voltage [32]. Moreover, the acoustic performances of the microspeaker could be influenced after the protection of chip by packaging [29]. The microspeaker designs in this study are to enhance the SPL at low frequencies. As demonstrated in existing headphones, the low-frequency and high-frequency speakers can be integrated by assembly to meet the bandwidth requirement. Thus, with respect to further improvement, it is possible to integrate the presented low-frequency microspeaker with high-frequency microspeaker by using the system-in-packaging (SiP) or system-on-chip (SoC) approaches to realize a full-range speaker. Furthermore, the increasing of diaphragm displacement will also improve the SPL in free field [7], and hence the presented designs can be extended to free field applications as well.

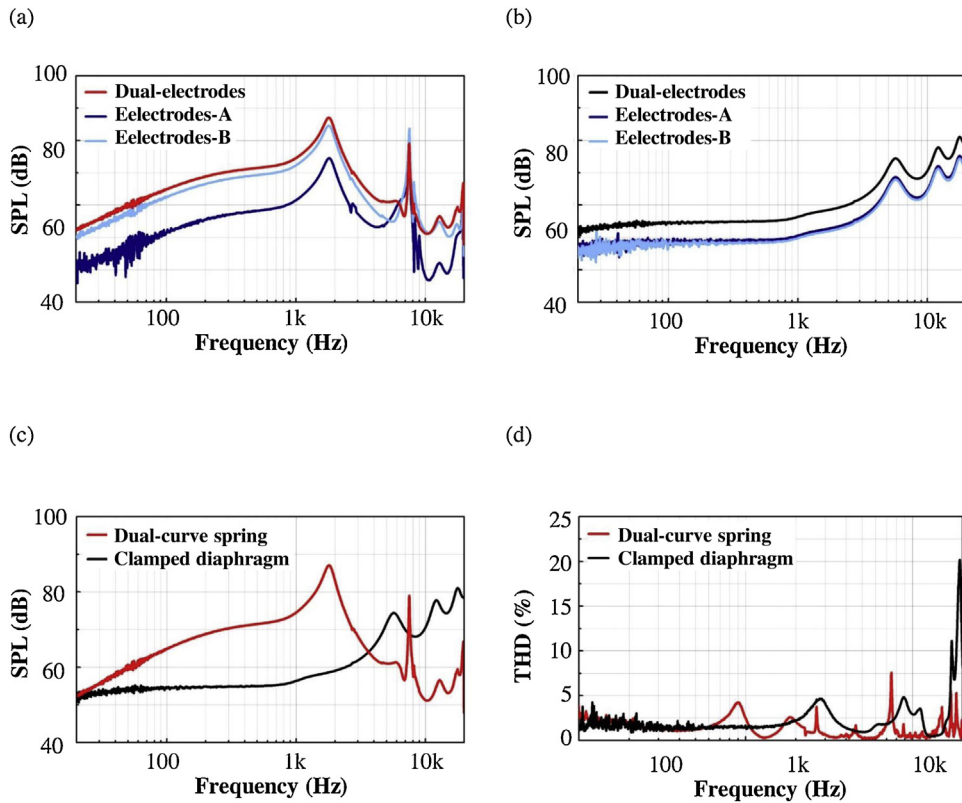


Fig. 16. Measured frequency responses of SPL (in the ear simulator) for the proposed dual-spring and the reference clamped microspeakers driven by dual electrodes (electrodes-A and electrodes-B) or single electrode (electrodes-A or electrodes-B), (a) the proposed dual-curve spring design, (b) the reference clamped diaphragm microspeaker, (c) the comparison of the above two SPL frequency responses with dual-electrode driving, and (d) the comparison of THD between the dual-curve spring and the clamped diaphragm microspeakers.

CRediT authorship contribution statement

Hsu-Hsiang Cheng: Conceptualization, Methodology, Writing - original draft. **Sung-Cheng Lo:** Visualization, Data curation, Writing - review & editing. **Zi-Rong Huang:** Methodology. **Yi-Jia Wang:** Investigation. **Mingching Wu:** Resources. **Weileun Fang:** Supervision, Writing - review & editing, Project administration.

Acknowledgements

This project was supported by the ministry of science and technology (MOST) of Taiwan under the grant number MOST 108-2911-I-007-508-, and MOST 108-2218-E-007-034-. The authors would also like to appreciate the Center of Nano Science and Technology at National Tsing Hua University, the Nano Facility Center at National Chiao Tung University, and the National Nano Device Laboratory of MOST for providing the fabrication facilities.

Appendix A. Supplementary data

Supplementary material related to this article can be found, in the online version, at doi:<https://doi.org/10.1016/j.sna.2020.111960>.

References

- [1] M.R. Douglass, Lifetime estimates and unique failure mechanisms of the Digital Micromirror Device (DMD), in: IEEE IRPS 1998, Reno, NV, USA, Mar. 31-Apr. 2, 1998, pp. 9–16.
- [2] SiTime, [online] Available: <http://www.sitime.com>.
- [3] Vesper, [online] Available: <https://vespermems.com>.
- [4] Knowles, [online] Available: <https://www.knowles.com>.
- [5] USound, [online] Available: <https://www.usound.com>.
- [6] Audio Pixels, [online] Available: <http://www.audiopixels.com.au>.
- [7] I. Shahhosseini, E. Lefevre, J. Moulin, E. Martinic, M. Woytasik, G. Lemarquand, Optimization and microfabrication of high performance silicon-based MEMS microspeaker, *IEEE Sens. J.* 13 (2013) 273–284.
- [8] M.-C. Cheng, W.-S. Huang, S.R.-S. Huang, A silicon microspeakers for hearing instruments, *J. Micromech. Microeng.* 14 (2004) 859–866.
- [9] S.-S. Je, J. Chae, A compact, low-power, and electromagnetically actuated microspeaker for hearing aids, *IEEE Electr. Device Lett.* 29 (2008) 856–858.
- [10] Y.-C. Cheng, Y.-T. Cheng, A low-power milliwatt electromagnetic microspeaker using a PDMS membrane for hearing aids application, in: *IEEE MEMS 2011*, Cancun, Mexico, January 23–27, 2011, pp. 1213–1216.
- [11] J.J. Neumann Jr., K.J. Gabriel, CMOS-MEMS membrane for audio-frequency acoustic actuation, *Sens. Actuators A* 95 (2002) 175–182.
- [12] G. De Pasquale, L. Rufer, S. Basrour, A. Somà, Modeling and validation of acoustic performances of micro-acoustic sources for hearing applications, *Sens. Actuators A* 274 (2016) 614–628.
- [13] H. Kim, A.A. Astle, K. Najafi, L.P. Bernal, P.D. Washabaugh, F. Cheng, Bi-directional electrostatic microspeaker with two large-deflection flexible membranes actuated by single/dual electrodes, in: *IEEE Sensors 2005*, Irvine, CA, USA, October 30–November 3, 2005, pp. 89–92.
- [14] S.C. Ko, Y.C. Kim, S.S. Lee, S.H. Choi, S.R. Kim, Micromachined piezoelectric membrane acoustic device, *Sens. Actuators A* 103 (2003) 130–134.
- [15] C. Luo, G.Z. Cao, I.Y. Shen, Development of lead-zirconate-titanate (PZT) thin-film microactuator probe for intracochlear applications, *Sens. Actuators A* 201 (2013) 1–9.
- [16] S.H. Yi, S.C. Ur, E.S. Kim, Performance of packaged piezoelectric microspeakers depending on the material properties, in: *IEEE MEMS 2009*, Sorrento, Italy, January 25–29, 2009, pp. 765–768.
- [17] S.S. Lee, R.M. White, Piezoelectric cantilever acoustic transducer, *J. Micromech. Microeng.* 8 (1998) 230–238.
- [18] F. Stoppel, A. Männchen, F. Niekiel, D. Beer, T. Giese, B. Wagner, New integrated full-range MEMS speaker for in-ear applications, in: *IEEE MEMS 2018*, Belfast, Northern Ireland, UK, January 21–25, 2018, pp. 1068–1071.
- [19] R.J. Littrell, High performance piezoelectric MEMS microphones, Ph.D. dissertation, The University of Michigan, 2010.
- [20] S.-J. Chen, Y. Choe, L. Baumgartel, A. Lin, E.S. Kim, Edge-released piezoelectric MEMS acoustic transducers in array configuration, *J. Micromech. Microeng.* 22 (2012), 025005.
- [21] H.-H. Cheng, Z.-R. Huang, S.-C. Lo, Y.-J. Wang, M.-C. Wu, W. Fang, Piezoelectric MEMS microspeaker with suspension springs and dual electrode to enhance

- sound pressure level, in: IEEE MEMS 2019, Seoul, Korea, January 27–31, 2019, pp. 767–770.
- [22] H.-H. Cheng, Z.-R. Huang, M.-C. Wu, W. Fang, Low frequency sound pressure level improvement of piezoelectric MEMS microspeaker using novel spiral spring with dual electrode, in: Transducers 2019, Berlin, Germany, Junuary 23–27, 2019, pp. 2013–2016.
- [23] K. Shin and S. Ko, "Multi-function micro speaker", US Patent No. 8,345,915.
- [24] S.-S. Je, N. Wang, H.C. Brown, D.P. Arnold, J. Chae, An electromagnetically actuated microspeaker with fully-integrated wax-bonded Nd-Fe-B micromagnets for hearing aid applications, in: Transducers 2009, Denver, CO, USA, Junuary 21–25, 2009, pp. 2013–2016.
- [25] F. Casset, R. Dejaeger, B. Laroche, B. Desloges, Q. Leclere, R. Morisson, Y. Bohard, J.P. Goglio, J. Escato, S. Fanget, A 256 MEMS membrane digital loudspeaker array based on PZT actuators, Proc. Eng. 120 (2015) 49–52.
- [26] F. Stoppel, C. Eisermann, S. Gu-Stoppel, D. Kaden, T. Glese, B. Wagner, Novel membrane-less two-way MEMS loudspeaker based on piezoelectric dual-concentric actuators, in: Transducers 2017, Kaohsiung, Taiwan, Junuary 18–22, 2017, pp. 2047–2050.
- [27] K.E. Petersen, Silicon as a mechanical material, Proc. IEEE 70 (1982) 420–457.
- [28] C.-I. Chang, M.-H. Tsai, C.-M. Sun, W. Fang, Development of CMOS-MEMS in-plane magnetic coils for application as a three-axis resonant magnetic sensor, J. Micromech. Microeng. 24 (2014), 035016.
- [29] J.R. Chang, C.N. Wang, Acoustical Analysis of Enclosure Design Parameters for Microspeaker System, J. Mechan. 35 (2019) 1–12.
- [30] M. Dekkers, H. Boschker, M. van Zalk, M. Nguyen, H. Nazeer, E. Houwman, G. Rijnders, The significance of the piezoelectric coefficient $d_{31,eff}$ determined from cantilever structures, J. Micromech. Microeng. 23 (2013), 025008.
- [31] Y. Tsujii, S. Kawabe, F. Kurokawa, H. Hida, I. Kanno, Comparison of effective transverse piezoelectric coefficient $e_{31,f}$ of Pb_{(Zr,Ti)O₃} thin films between direct and converse piezoelectric effects, Japanese J. Appl. Phys. 54 (2015), 10NA04.
- [32] X.J. Lou, J. Wang, Bipolar and unipolar electrical fatigue in ferroelectric lead zirconate titanate thin films: an experimental comparison study, J. Appl. Phys. 108 (2010), 034104.

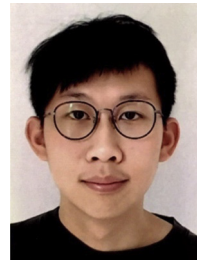
Biographies



Hsu-Hsiang Cheng was born in Taichung, Taiwan. In 2017, he received his B.S. degree from the Department of Power Mechanical Engineering, National Tsing Hua University, Taiwan. In 2019, he received his M.S. degree from the Department of Power Mechanical Engineering, National Tsing Hua University, Taiwan. His research interests include design and implementation of the piezoelectric MEMS microspeakers for SPL and frequency range improvement, and fabrication of the SOI process with piezoelectric thin film.



Sung-Cheng Lo was born in Taoyuan, Taiwan. He received the M.S. degree from the Mechanical Engineering Department, Ming Chi University of Technology, New Taipei, Taiwan, in 2010. He is currently pursuing the Ph.D. degree at the Power Mechanical Engineering Department, National Tsing Hua University, Hsinchu, Taiwan. He is currently involved in development of condenser microphone, piezoelectric microphone, piezoelectric micro speaker and bone conduction microphone. His current research interests include advanced MEMS process, acoustic micro device, motion sensors, optical scanning mirrors, MEMS micro sensors, and processes integration.



Zi-Rong Huang was born in Taipei, Taiwan. In 2016, he received his B.S. degree from Mechanical Engineering, Chang Gung University, Taiwan. In 2018, he received his M.S. degree from the Department of Power Mechanical Engineering, National Tsing Hua University. His research interests include design and implementation of piezoelectric MEMS microphone for SNR ratio and sensitivity enhancement. He is currently involved in the design of bolometer for thermal image.



Yi-Jia Wang was born in Taichung, Taiwan. In 2017, he received his B.S. degree from the Department of Power Mechanical Engineering, National Tsing Hua University, Taiwan. He is currently a M.S. student in the Department of Power Mechanical Engineering, National Tsing Hua University, Taiwan. He is currently involved in design, microfabrication and implementation of the piezoelectric MEMS microspeakers for bandwidth and SPL enhancement.



Mingching Wu was born in Taoyuan, Taiwan. He received the Ph.D. degree in power mechanical engineering (PME) in 2005 from the National Tsing-Hua University, Taiwan. He has been working in the MEMS field for 20 years and his research interests include Si based micromachining process, MEMS sensors, and optical scanning mirror. In 2007, he joined the R&D division in Asia Pacific Microsystems, Taiwan, and developed the 3-axis accelerometer. In 2009, the product is successfully commercialized and to be the first 3-axis MEMS accelerometer in Taiwan. In 2013, he founded GlobalMEMS Co., Ltd. To development various MEMS sensors by using piezoelectric MEMS technology included MEMS Mic and industrial accelerometers. He is working for CoretronicMEMS and intends to develop MEMS scanning mirror for LiDAR application now.



Weileun Fang was born in Taipei, Taiwan. He received his Ph.D. degree from Carnegie Mellon University in 1995. His doctoral research focused on the determining of the mechanical properties of thin films using micromachined structures. In 1995, he worked as a postdoctoral research at Synchrotron Radiation Research Center, Taiwan. He joined the Power Mechanical Engineering Department at the National Tsing Hua University(Taiwan)in 1996, where he is now a Chair Professor as well as a faculty of NEMS Institute. In 1999, he was with Prof. Y.-C. Tai at California Inst. Tech. as a visiting associate. He became the IEEE Fellow in 2015 to recognize his contribution in MEMS area. His research interests include MEMS with emphasis on micro fabrication/packaging technologies, CMOS MEMS, CNT MEMS, micro optical systems, micro sensors and actuators, and characterization of thin film mechanical properties. He is now the Chief Editor of JMM, the Associate Editor of IEEE Sensors Journal, and the Board Member of IEEE Transactions on Device and Materials Reliability. He served as the member of ISC (International steering committee) of Transducers in 2009–2017, and the ISC chair in 2017–2019. He also served as the General Chair of Transducers Conference in 2017. He was the TPC of IEEE MEMS and EPC of Transducers for many years, and the Program Chair of IEEE Sensors Conference in 2012. He served as the Chief Delegate of Taiwan for the World Micromachine Summit (MMS) in 2008–2012, and the General Chair of MMS in 2012. Prof. Fang has close collaboration with MEMS industries and is now the VP of MEMS and Sensors Committee of SEMI Taiwan.